Electric Power Systems Research 189 (2020) 106772

Contents lists available at ScienceDirect

Electric Power Systems Research

journal homepage: www.elsevier.com/locate/epsr

Voltage stability assessment accounting for current-limited converters☆

Bahtiyar Can Karatas*[a], Moumita Sarkar[b], Hjörtur Jóhannsson[a], Arne Hejde Nielsen[a], Poul Ejnar Sørensen[b]

[a] Department of Electrical Engineering, Technical University of Denmark, Denmark
[b] Department of Wind Energy, Technical University of Denmark, Denmark

ARTICLE INFO

Keywords:
Power system analysis computing
Power system stability
Thévenin equivalent
Real-time assessment
Wide-area monitoring

ABSTRACT

This paper investigates how current-limited converters influence system stability. An improved approach for assessing voltage stability is introduced, which determines the maximum deliverable power to a load by accounting for changes in the Thévenin voltages. The new approach is able to detect voltage instability well before the traditional approach based on Thévenin impedance matching. A new stability boundary is discovered that describes the aperiodic small signal stability boundary for current-limited converters. The improved approach was modified to account for current-limited converters. The detection of voltage and rotor angle instability during current limitation were demonstrated on a seven bus system, where test cases were performed. The test cases showed that voltage instability can lead to aperiodic small signal instability, when the converter has reached its current limit and loss of synchronism in the unstable region during current-limitation causes the system voltages to collapse.

1. Introduction

Thévenin equivalent computations are used in a variety of stability assessment methods including aperiodic small-signal stability of generators and long-term voltage stability of loads. In [1] an active power margin is proposed, which is used to monitor the steady-state torque balance of each generator in the power system. In [2,3] the maximum deliverable power to non-controlled loads is determined by accounting for how variations in the load impedance are reflected in the contributing generator angles. Both of these methods depend on fast and efficient computation of Thévenin equivalents, in order to compute the stability boundaries in real-time.

The availability of Phasor Measurement Units (PMUs) [4,5] throughout a power system provides full system observability, where complex bus voltages and complex branch currents can be obtained at a repetition rate equal to the system frequency. Additionally, by obtaining information about the system topology, Thévenin equivalent methods can be applied for real-time stability assessment.

The behaviour of Renewable Energy Sources (RES) during stressed system conditions introduce new challenges in assessing power system stability. Traditional offline approaches become insufficient in ensuring secure and stable operation. Therefore new approaches and methods are needed that are capable of assessing system stability of power systems with a larger share of RES. Research has been conducted that focused on assessing system stability and security in real-time [6–10]. In [1,11,12] algebraic derived expressions laid the foundation for an assessment method that monitors the steady state torque balance of each individual generator in a system. The results obtained from [13] enabled computation of Thévenin equivalents in milliseconds.

In [14] the Thévenin equivalent method together with sensitivity analysis were found most suitable for real-time assessment. The limitations of the Thévenin equivalent approach were addressed, which involved that the Thévenin voltage seen from the load remains constant as the load impedance varies. In [15,16] local phasor measurements are used to estimate the ThE̤venin equivalent seen from a load to detect voltage instability based on the ThE̤venin impedance matching criterion. The method iteratively estimates the ThE̤venin equivalent parameters based on how the load impedance changes until a specific threshold is met.

In previous work [17] a method was proposed to estimate how current-limited wind farms affect real-time voltage stability assessment. In [18] it was discovered that the impact of current-limited converters can be estimated prior to reaching the rated current. This paper investigates how current-limited converters affect system stability by using Thévenin equivalents. A previous improved approach for assessing voltage stability [2] is expanded to include current-limited

☆ Submitted to the 21st Power Systems Computation Conference (PSCC 2020).

* Corresponding author.
E-mail address: bcakrts@gmail.com (B.C. Karatas).

https://doi.org/10.1016/j.epsr.2020.106772
Received 1 October 2019; Received in revised form 17 April 2020; Accepted 2 August 2020
Available online 10 August 2020
0378-7796/

converters. The approach takes into account the changes in the Thévenin voltage magnitude seen from a load with respect to load impedance changes.

The structure of the paper is as follows. Section 2 describes the improved voltage stability approach. Section 3 describes the derivation of lines of constant current and the discovery of a aperiodic small signal stability boundary for current-limited converters, which appears as a horizontal line in the injection impedance plane. In Section 4 the new stability boundary is validated based on two time-domain simulations performed in PSS®E and finally in Section 5 the paper is concluded.

2. Improved voltage stability approach

To determine the maximum deliverable power to a non-controlled load by accounting for changes in Thévenin voltages, the following two assumptions are necessary:

- Power is injected into nodes of constant voltage magnitude. The synchronous generators are represented as a voltage source $V\angle\delta$ and depending on the excitation system, the voltage source is directly connected to the generator terminals if an Automatic Voltage Regulator (AVR) is present, or the voltage source is connected behind the synchronous reactance X_d. In the latter case, the generator is manually excited or the Over-Excitation Limiter (OXL) has been activated.
- The second assumption is that loads are represented by their impedance values. The approach needs the instantaneous representation of the system conditions in order to correctly determine the changes in Thévenin voltages seen from the load.

These assumptions are valid by receiving PMU-snapshots at a high repetition rate. Based on the assumptions power injections are represented into nodes of constant voltage magnitude and loads by their impedances with a constant load angle. This means only two degrees of freedom are needed to determine the maximum deliverable power to the load and they are the change in generator rotor angles with respect to load impedance magnitude changes.

Based on the superposition principle the complex Thévenin voltage seen from a non-controlled load can be decomposed into the voltages of contributing generators scaled by complex coefficients. This can be visualized in Fig. 1. Each of the complex coefficients are independent of the load impedance and only depend on the network topology. Considering the Thévenin equivalent seen from a voltage-controlled node seen in Fig. 2, an expression for the generator rotor angle δ_{vc} can be derived:

$$\delta_{vc} = \arccos\left(\frac{V_{vc}^2 \cos\phi_{th,vc} - P_{inj} Z_{th,vc}}{E_{th,vc} V_{vc}}\right) + \theta_{th,vc} - \phi_{th,vc} \tag{1}$$

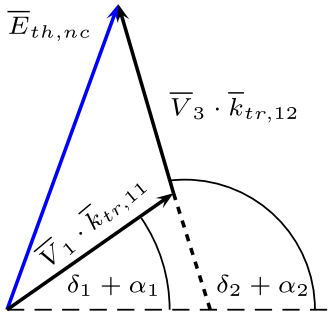

Fig. 1. Phasor diagram illustrating the superposition principle of determining the complex Thévenin voltage seen from a non-controlled load.

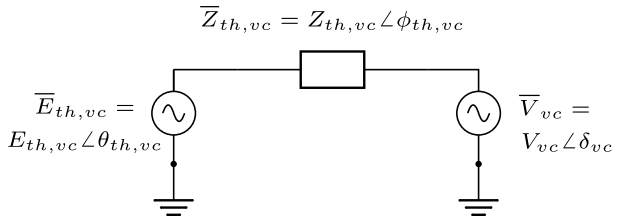

Fig. 2. Thévenin equivalent seen from a generator, which is used to estimate how the generator angle δ_{vc} behaves with respect to load impedance changes Z_{load}.

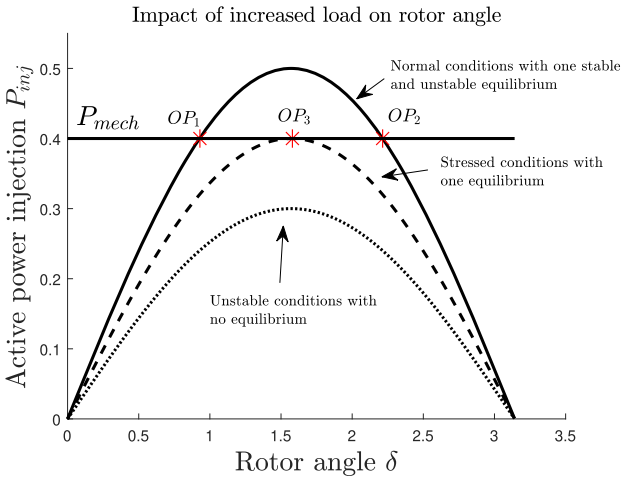

Fig. 3. $P-\delta$ curves for three scenarios: For the solid characteristic, the line of constant P_{mech} intersects twice, where the left hand side represents stable operation. For the dashed characteristic, P_{mech} intersects exactly once and for the dotted characteristic it never intersects.

Assuming that a generator operates with constant mechanical input power and the load angle is fixed, the only variable influencing the rotor angle δ_{vc} is the changes in load impedance magnitude Z_{load}, where each change represents a different Thévenin equivalent seen from the generator. This can be visualized by $P-\delta$ curves as seen in Fig. 3.

Each change in load impedance magnitude can be represented by one of three scenarios. In the first case the solid curve intersects twice with the line of constant mechanical input power, where OP_1 represents a stable operating point and OP_2 represents an unstable operating point. In the second case the dashed curve only intersects once, which represents the critical point for δ_{vc} and it is represented as OP_3. In the third case the dotted curve does not intersect and no equilibrium exists for the generator.

For the non-controlled load an interval is defined from the actual load impedance to the Thévenin impedance seen from the load in evenly spaced points. Each point, when evaluated, represents a new Thévenin equivalent seen from the contributing generators, which is used to estimate the change in rotor angles by using (1). The estimated rotor angles are then used to estimate the Thévenin voltage seen from the non-controlled load. The maximum deliverable power can be estimated by using (2), which is derived from the two bus Thévenin equivalent seen from a load in Fig. 5:

$$P_{load} = I_{load}^2 \Re(\overline{Z}_{load}) = \left|\frac{\overline{E}_{th,nc}(\overline{Z}_{load})}{\overline{Z}_{th,nc} + \overline{Z}_{load}}\right|^2 R_{load} \tag{2}$$

At some point during the interval the maximum deliverable power to the load will start to decline or a contributing generator's angle becomes imaginary, which means the point of maximum deliverable power to the load has been reached. This method increases in accuracy

Input : PMU-snapshot of the system conditions
Determine complex coefficients $\overline{k}_{tr}$ for each nc load **foreach** *nc load* **do**
  foreach *change in* Z_{load} **do**
    Determine the stability condition of the generator operating point using
    Determine $\overline{E}_{th,nc}$ using superposition
  end
  Estimate maximum deliverable power to the load $P_{load,\max}$ according to
end

Algorithm 1. Proposed voltage stability approach.

as the non-controlled load moves closer to the point of maximum deliverable power, because the interval becomes smaller. The above described approach is summarized by Algorithm 1.

To illustrate the improved voltage stability approach, the seven bus wind system shown in Fig. 4 is analyzed.

Generator G_1 represents aggregated Type IV wind turbines that maintain local voltage control and prioritize active power injection, which is similar to a synchronous generator with an AVR that maintains a constant voltage magnitude at the terminals. The model is based on a variable speed 2.3 MW developed by Siemens in PSS®E. Generator G_2 represents an infinite machine. The load is represented at the high-voltage side of the On-Load Tap Changer (OLTC) transformer to include losses. Based on the assumption that power is injected into nodes of constant voltage magnitude and the load angle is fixed, information about the possible operating points for the grid-side converter are obtained by determining the phase angle difference between the two generators in the system with respect to load impedance magnitude changes. Based on the initial conditions, the active power injection of G_1 (red) and the load power P_{load} (blue) can be visualized as contour plots as seen in Fig. 6.

The contour of $P_{G1} = 13.8$ MW represents the trajectory of possible operating points for the grid-side converter and the initial operating point is represented as point *A*, which intersects with the initial load power $P_{load} = 38$ MW. The black dash dotted line represents the maximum injectable power when the load impedance magnitude is fixed. The black horizontal line represents the voltage stability boundary based on the Thévenin impedance matching approach, where the load impedance magnitude Z_{load} equals the magnitude of the Thévenin impedance. The black horizontal line assumes that the Thévenin voltage magnitude seen from the load remains constant with respect to load impedance magnitude changes. Using the approach described in Algorithm 1 the point of maximum deliverable power to the load is represented as point *B*, which takes into account how the Thévenin voltage seen from the load changes with respect to load impedance magnitude changes. Based on the initial conditions the horizontal line and the improved voltage stability approach would be able to detect voltage instability. Initially the actual operating point is far away from the voltage stability boundary.

3. Improved voltage stability approach including current-limited converters

3.1. Lines of constant current

To derive expressions for current-limited converters the two-bus Thévenin equivalent seen from a current source in Fig. 7 is considered.

To derive an expression for lines of constant current the following expressions are used:

$$V_{vc} = E_{th,vc} - Z_{th,vc} I_c \tag{3}$$

$$Z_{inj} = \frac{V_{vc}}{I_c} \tag{4}$$

By inserting (4) into (3) and rearranging the terms, the following equation of a circle of constant current in the injection impedance plane is derived:

$$(R_{inj} - a)^2 + (X_{inj} - b)^2 = r^2 \tag{5}$$

with center coordinates (a, b) and radius r:

$$(a, b) = (-R_{th,vc}, -X_{th,vc}) \tag{6}$$

$$[10pt] r = \frac{E_{th,vc}}{I_c} \tag{7}$$

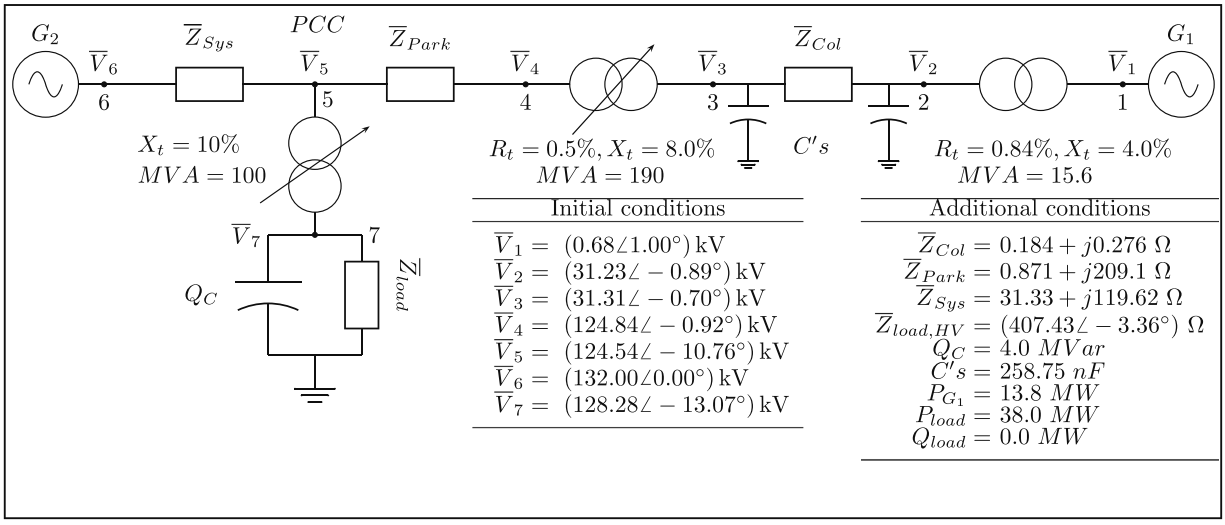

Fig. 4. Seven bus system used for testing current-limited operation of the grid-side converter of the wind farm represented by G_1. The load at bus 7 is represented as the complex impedance $\overline{Z}_{load}$ and generator G_2 represents an infinite bus ($H \to \infty$) with a constant voltage magnitude at its terminal.

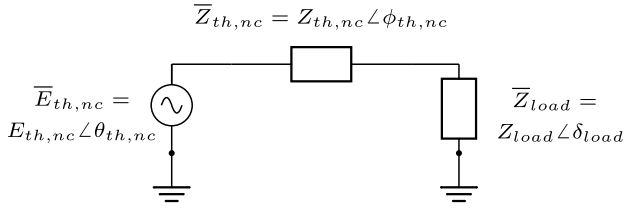

Fig. 5. Thévenin equivalent seen from a non-controlled load, which is used for estimating how $E_{th,nc}$ behaves with respect to the load impedance Z_{load}.

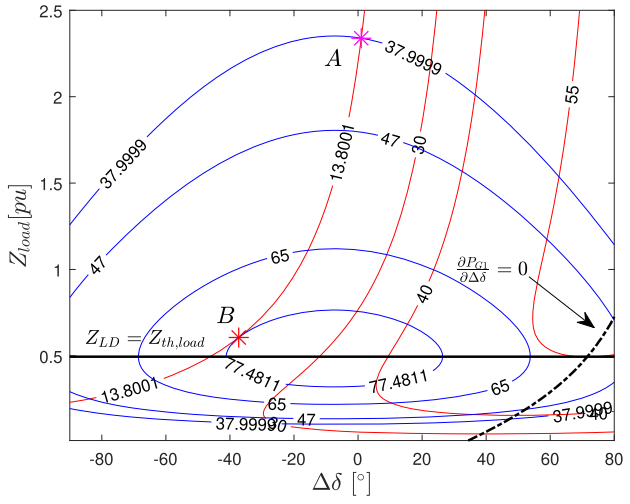

Fig. 6. Contours of constant injected active power P_{G1} (red) and constant delivered power to the load P_{load} (blue) in the $\Delta\delta - Z_{load}$ plane. Point A represents the initial operating point. Point B represents the maximum deliverable power to the load. (For interpretation of the references to colour in this figure legend, the reader is referred to the web version of this article.)

3.2. Maximum injectable power during current-limited operation

In [11] the following expression for lines of constant active power was derived, which can be determined from a two bus Thévenin equivalent:

$$(R_{inj} - a)^2 + (X_{inj} - b)^2 = r^2 \tag{8}$$

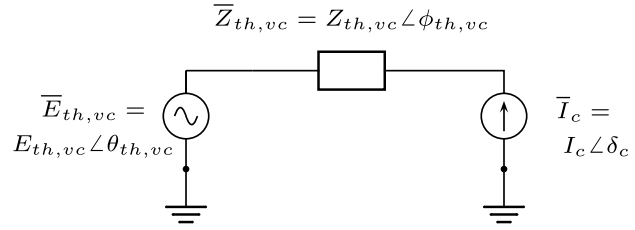

Fig. 7. Simple two bus Thévenin equivalent seen from a current source. This system is used to derive characteristic curves and critical lines in the injection impedance plane.

with center coordinates (a, b) and radius r:

$$(a, b) = \left(-R_{th,vc} + \frac{E_{th,vc}^2}{2P_{inj}},\ -X_{th,vc}\right) \tag{9}$$

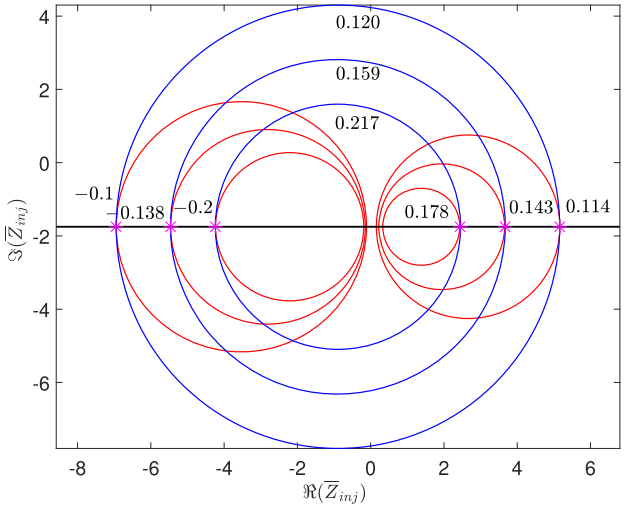

Fig. 8. Lines of constant current magnitudes represented as blue circles and lines of constant injected and absorbed power represented as red circles. For each constant current magnitude circle, there exists a red circle representing the maximum injectable or absorbed power, which intersects exactly once on the line of $-X_{th,vc}$. (For interpretation of the references to colour in this figure legend, the reader is referred to the web version of this article.)

$$[10pt] r = \sqrt{\frac{E_{th,vc}^4 - 4E_{th,vc}^2 R_{th,vc} P_{inj}}{4P_{inj}^2}} \tag{10}$$

It is worth noticing that the center coordinates for circles of constant active power and circles of constant current lie on the same line – $X_{th,vc}$. Fig. 8 shows circles of constant current (blue) and circles of constant active power (red). Assuming that the grid-side converter is current-limited, there exists a circle of constant active power that intersects exactly once with a circle of constant current, which is highlighted as the purple intersections. Each of the red circles represent the maximum injectable active power or absorbed active power for a constant current magnitude and they intersect on the line – $X_{th,vc}$. The black horizontal line represents the aperiodic small signal stability boundary for current-limited converters, where operation below the line represents stable operation and operation above the line represents unstable operation.

3.3. Visualizing operating points in the normalized impedance plane

The converter operating points can be visualized in the normalized injection impedance plane by shifting each operating point with the value of $\overline{Z}_{th,vc}$ and normalizing with the radius of the circle of constant current:

$$r = \frac{E_{th,vc}}{I_{c,\max}} \tag{11}$$

$$\overline{Z}_{inj,norm} = \frac{\overline{Z}_{inj} + \overline{Z}_{th,vc}}{r} \tag{12}$$

By using (12), the current-limited operating points are mapped into the normalized injection impedance plane, where the unit circle represents the condition of constant current magnitude and the black horizontal line represents the aperiodic small signal stability boundary going through the origin.

3.4. Voltage stability approach including current-Limited converters

The voltage stability approach described in Algorithm 1 is based on voltage controlled nodes. The same approach can be applied to Type IV wind turbines that maintain local voltage control and prioritize active power injection. When the converter reaches its current limitation, the approach must be modified accordingly. Based on the two bus Thévenin equivalent seen from a current source in Fig. 7, the current angle δ_c can be determined as:

$$\delta_c = \theta_{th,vc} - \arccos\left(\frac{P_{inj} - I_c^2 Z_{th,vc}\cos(\phi_{th,vc})}{V_{th,vc} I_c}\right) \tag{13}$$

Based on the superposition principle for determining the Thévenin equivalent seen from a non-controlled load, the voltage of contributing generators were scaled by a complex coefficient. In case of current-limited operation, the contribution is determined as the impedance times the current. Assuming that active power injection is prioritized and the load angle is fixed, the only variable influencing the current limited converter angle δ_c is the load impedance magnitude Z_{load}. Each variation in Z_{load} represents a new Thévenin equivalent and the equilibrium of the angle can be determined. The stable current angles are then used to estimate the Thévenin voltage seen from the load in order to determine the maximum deliverable power to the load, similar to Algorithm 1.

3.5. Reactive power capability of Type IV wind turbine based wind farms

The reactive power capability of a converter connected Type IV wind turbine is dependent on the wind turbine terminal voltage and active power production. For wind farms consisting of several wind turbines and power collection cables, aggregated reactive power capability model has been developed in Sarkar et al. [19]. In this model a single wind turbine representation of Type IV wind turbine has been used together with equivalent impedance of power collection system. This model also includes the susceptance of power collection cables to give a realistic estimation of reactive power capability of wind farms. In this paper, the approach is used to calculate the reactive power limit of the aggregated wind farm G_1 in Fig. 4. The voltage limited reactive power capability of the wind farm, Q_V, can be derived from the following equation:

$$Q_V = \sqrt{\left(\frac{V_G V_C^{\max}}{|\overline{Z}_{eq}|}\right)^2 - \left(P + \frac{V_G^2 R_{eq}}{|\overline{Z}_{eq}|^2}\right)^2} - \frac{V_G^2 X_{eq}}{|\overline{Z}_{eq}|^2} \tag{14}$$

where, V_G is the voltage at the point of connection of wind farm, $V_C^{\max}$ is the maximum allowable converter voltage, P is active power production from wind farm and $\overline{Z}_{eq}$ is the sum of impedance of aggregated collection system cables, individual wind turbines and wind turbine transformers. The current limited reactive power capability, Q_I, can be derived from:

$$Q_I = \sqrt{(V_G I_C^{\max})^2 - P^2}. \tag{15}$$

where, $I_C^{\max}$ is the maximum allowable current from the converter. At any operating point, the reactive power capability of a wind farm can be either voltage limited or current limited. The maximum reactive power injection capability of a wind farm can be derived from the following expression:

$$Q_{lim} = \min(Q_V, Q_I) + B_{eq} V_G^2, \tag{16}$$

where, B_{eq} is the equivalent shunt susceptance of collection system cables. Detailed description of the model and methodology is given in Sarkar et al. [19].

4. Simulation results

4.1. Voltage instability during current-limited operation

A time domain simulation was performed in PSS®E of the seven-bus wind system given in Fig. 4. To provoke voltage instability the active load power at bus 7 was manually increased from 38 MW to 62 MW over a time period of 111 s. At $t = 35$ s the OLTC transformer started tap-changing to keep the voltage constant at the low-voltage side. Each increase in load power moved the actual operating point closer to the voltage stability boundary. The first plot in Fig. 9 shows the bus voltage magnitudes of the high- and low voltage side of the OLTC-transformer, the second and third plot show the voltage and current magnitude at the converter terminals. The fourth plot shows the reactive power injection and the maximum reactive power injection computed using (16). Eventually at $t = 111$ s (snapshot *I*) the grid-side converter cannot maintain a constant voltage magnitude at the terminals and becomes current-limited. The last two tap-changes of the OLTC-transformer pushes the system voltages further down, which leads to the actual operating point becoming voltage unstable at $t = 205.6$ s (snapshot *II*). This can be seen in Fig. 10 as point *A*. Beyond this point the system voltages continue falling and the system conditions are worsening.

Fig. 11 shows the converter operating points mapped into the normalized injection impedance plane. The unit circle represents the condition of constant current magnitude and the black horizontal line represents the aperiodic small-signal stability boundary during current-limited operation. Operation below the black line represents stable operation and operation above represents unstable operation. It can be

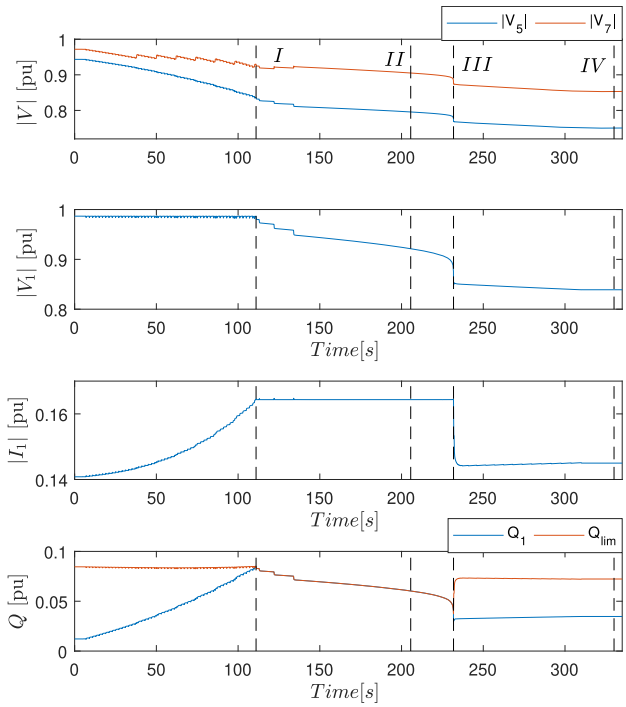

Fig. 9. The first plot shows the bus voltage magnitudes of the OLTC-transformer. The second and third plot show the voltage and current magnitude of the grid-side converter. The fourth plot shows the reactive power and the maximum reactive power. At snapshot *I* the grid-side converter becomes current-limited. At snapshot *II* the voltage stability boundary is crossed. At snapshot *III* the wind turbines enter FRT-mode and at snapshot *IV* the system has stabilized.

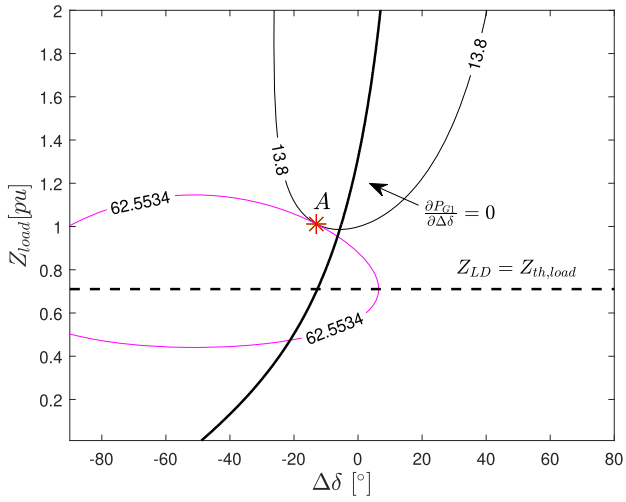

Fig. 10. Contours of constant injected active power P_{G1} (black) and constant delivered power to the load P_{load} (purple) in the $\Delta\delta - Z_{load}$ plane at $t = 205.6s$. The actual operating point has reached the point of maximum deliverable power to the load. (For interpretation of the references to colour in this figure legend, the reader is referred to the web version of this article.)

seen that after the actual operating point becomes voltage unstable, the converter keeps increasing its angle while maintaining a constant current magnitude and eventually at $t = 231.4$ s, the normalized operating point for the converter crosses the aperiodic small signal stability boundary. At the same time the converter enters Fault-Ride Through (FRT) mode and prioritizes reactive power injection and reduced the active power injection. Because the converter terminal voltage is below 0.9 pu, the wind turbines should be disconnected according to the grid

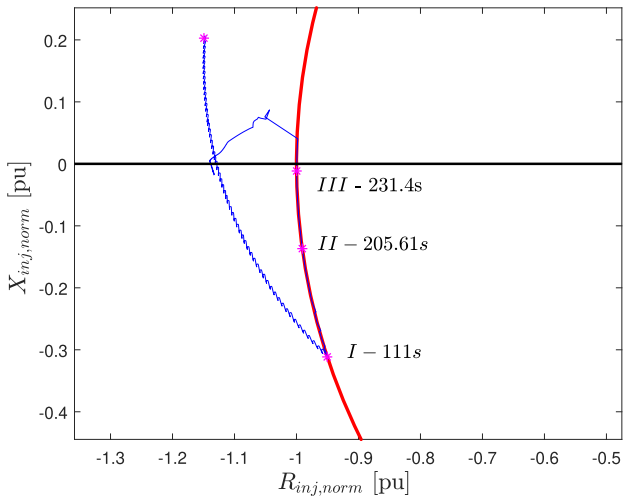

Fig. 11. Converter operating points (blue) mapped into the normalized injection impedance plane. At snapshot *I* the grid-side converter becomes current-limited. At snapshot *II* the voltage stability boundary is crossed. At snapshot *III* the aperiodic small-signal stability boundary is crossed. (For interpretation of the references to colour in this figure legend, the reader is referred to the web version of this article.)

codes. This test case showed the voltage instability can lead to aperiodic small signal instability for current-limited converters.

4.2. System blackout during current-limited operation

For the second test case the initial conditions have been modified for the seven bus system. The aggregated wind turbines have been scaled to 40 units that corresponds to $P_{inj} = 92$ MW and the step-up transformer has also been scaled accordingly. The active load power has been increased to $P_{load} = 125$ MW and the shunt reactor to $Q_C = 70$ MVar. The first plot in Fig. 12 shows the bus voltage magnitudes at the high- and low voltage side of the OLTC-transformer, the second plot and third plot show the voltage and current magnitude at the converter terminals. To push the converter to its current limitation the actual load power is increased to 152 MW over a period of 317 s. Fig. 13 shows the mapped operating points (black) for the converter into the normalized injection impedance plane. The red circle represents the condition of constant current magnitude. It can be seen that the converter keeps increasing reactive power injection and converter operating point eventually reaches its current limitation at $t = 317$ s (snapshot *I*). The actual operating point is in the unstable region defined by the black horizontal line. The instant the converter is not able to maintain a constant voltage magnitude and switches to constant current magnitude, the system voltages collapse immediately due to the fast acting power converters. Fig. 14 shows contours of constant injected power P_{G1} (black) and constant delivered power to the load P_{load} (purple) at $t = 317$ s, when the converter becomes current-limited. It can be seen that the actual operating point has crossed the voltage stability boundary and the aperiodic small-signal stability boundary, which results in the collapse of system voltages.

5. Conclusion

This paper presented an improved approach for assessing voltage stability for current-limited converters. The approach takes into account how load impedance changes are reflected in the converter angle δ_c, in order to determine the maximum deliverable power to the load. A new stability boundary describing aperiodic small signal stability for current-limited converters was discovered. The boundary appears as a straight line in the normalized injection impedance plane. Two test cases were used to validate the stability boundary. The test cases

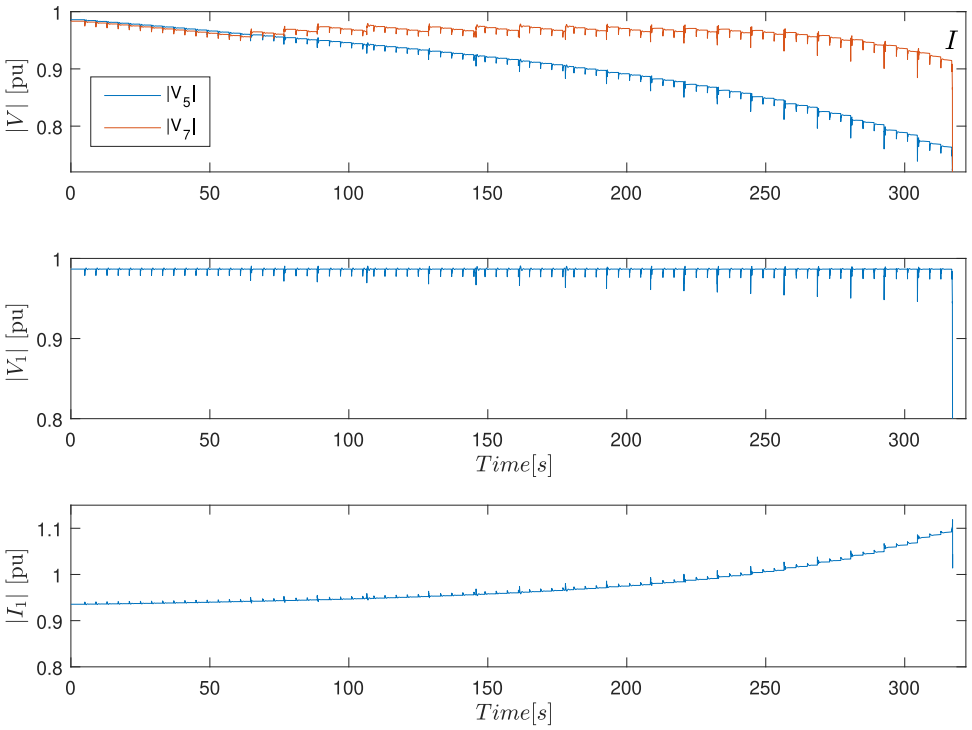

Fig. 12. The first plot shows the bus voltage magnitudes of the OLTC-transformer. The second and third plot show the voltage and current magnitude of the grid-side converter. At snapshot *I* the grid-side converter becomes current-limited and the system voltages collapse.

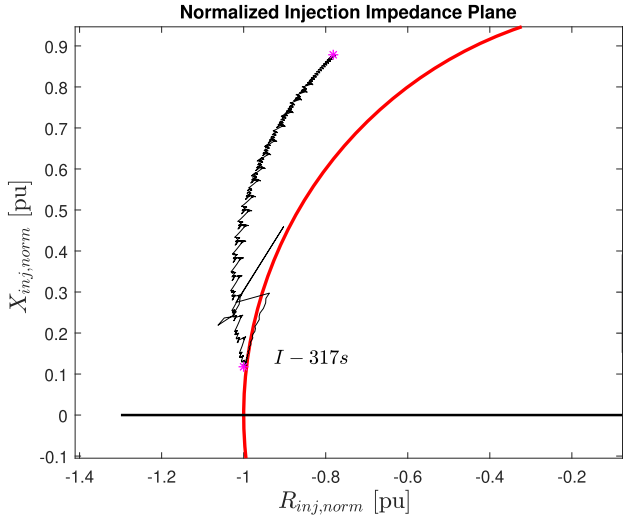

Fig. 13. Converter operating points (black) mapped into the normalized injection impedance plane. At snapshot *I* the grid-side converter becomes current-limited in the unstable region and the system voltages collapse immediately due to the fast acting converters.

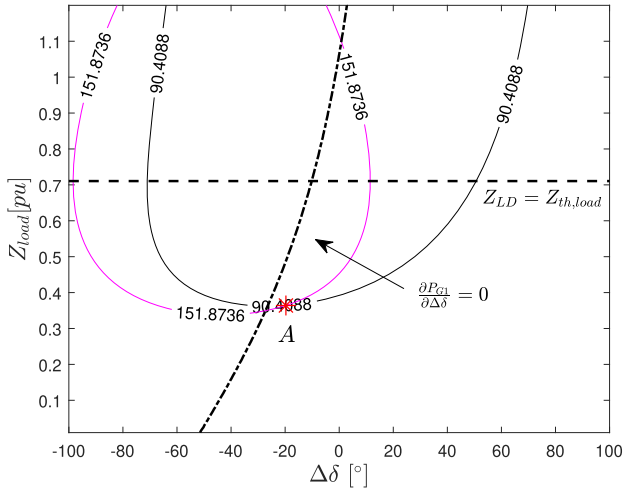

Fig. 14. Contours of constant injected active power P_{G1} (black) and constant delivered power to the load P_{load} (purple) in the $\Delta\delta - Z_{load}$ plane at $t = 317$ s. The grid-side converter is current-limited and the actual operating point has already crossed the voltage stability boundary and the aperiodic small-signal stability boundary. (For interpretation of the references to colour in this figure legend, the reader is referred to the web version of this article.)

showed that voltage instability was detected during current-limited operation, which lead to aperiodic small signal instability of the converter. The converter entered FRT-mode and prioritized reactive power injection and lowered active power injection. According to the grid codes the wind turbines would have been disconnected, because the terminal voltages did not recover. The test cases also showed that when the converter reaches its current limit in the unstable region, defined by the aperiodic small signal stability boundary, the system voltages collapse. Both test cases show that current-limited operation pushes the actual operating points closer to the stability boundaries, making the system more susceptible to instability.

Declaration of Competing Interest

The authors declare that they have no known competing financial interests or personal relationships that could have appeared to influence the work reported in this paper.

References

[1] H. Jóhannsson, A.H. Nielsen, J. Østergaard, Wide-area assessment of aperiodic small signal rotor angle stability in real-time, Proceedings of 2014 IEEE PES General Meeting, 28 (2013), pp. 4545–4557, https://doi.org/10.1109/TPWRS.2013.2271193.

[2] B.C. Karatas, H. Jóhannsson, A.H. Nielsen, Improved voltage stability boundary monitoring by accounting for variations in Thevenin voltage magnitude, Proceedings of 8th IEEE PES Innovative Smart Grid Technologies Conference, (2018), pp. pp.1–6, https://doi.org/10.1109/ISGTEurope.2018.8571648.
[3] C.H.L. Jørgensen, B. Can Karatas, H. Jóhannsson, S. Sommer, Binary search and fit algorithm for improved voltage stability boundary monitoring, Proceedings of 9th IEEE PES Innovative Smart Grid Technologies Conference, (2019).
[4] J. De La Ree, V. Centeno, J.S. Thorp, A.G. Phadke, Synchronized phasor measurement applications in power systems, IEEE Trans. Smart Grid 1 (1) (2010) 20–27, https://doi.org/10.1109/TSG.2010.2044815.
[5] A.G. Phadke, T. Bi, Phasor measurement units, WAMS, and their applications in protection and control of power systems, J. Mod Power Syst. Clean Energy 6 (4) (2018) 619–629, https://doi.org/10.1007/s40565-018-0423-3.
[6] H. Morais, P. Vancraeyveld, A.H.B. Pedersen, M. Lind, H. Johannsson, J. Ostergaard, SOSPO-SP: secure operation of sustainable power systems simulation platform for real-time system state evaluation and control, IEEE Trans. Ind. Inf. (2014), https://doi.org/10.1109/TII.2014.2321521.
[7] M. Glavic, T. Van Cutsem, Wide-area detection of voltage instability from synchronized phasor measurements. Part I: principle, IEEE Trans. Power Syst. 24 (3) (2009) 1417–1425, https://doi.org/10.1109/TPWRS.2009.2023272.
[8] M. Glavic, T. Van Cutsem, Wide-area detection of voltage instability from synchronized phasor measurements. Part II: simulation results, IEEE Trans. Power Syst. 24 (3) (2009) 1417–1425, https://doi.org/10.1109/TPWRS.2009.2023272.
[9] R. Diao, K. Sun, V. Vittal, R.J. O'Keefe, M.R. Richardson, N. Bhatt, D. Stradford, S.K. Sarawgi, Decision tree-based online voltage security assessment using PMU measurements, IEEE Trans. Power Syst. (2009), https://doi.org/10.1109/TPWRS.2009.2016528.
[10] I. Smon, S. Member, G. Verbic, Local voltage-stability index using tellegen's theorem, Power 21 (3) (2006) 1267–1275, https://doi.org/10.1109/TPWRS.2006.876702.
[11] H. Jóhannsson, J. Østergaard, A.H. Nielsen, Identification of critical transmission limits in injection impedance plane, Int. J. Electr. Power Energy Syst. (2012), https://doi.org/10.1016/j.ijepes.2012.05.050.
[12] H. Jóhannsson, Development of Early Warning Methods for Electric Power Systems, Technical University of Denmark, Department of Electrical Engineering, 2011 Ph.D. thesis.
[13] S. Sommer, H. Johannsson, Real-time Thevenin impedance computation, 2013 IEEE PES Innovative Smart Grid Technologies Conference, ISGT 2013, (2013), https://doi.org/10.1109/ISGT.2013.6497824.
[14] A. Perez, H. Jóhannsson, P. Vancraeyveld, J. Østergaard, Suitability of voltage stability study methods for real-time assessment, IEEE PES ISGT Europe, (2013), pp. 1–5.
[15] S. Corsi, G.N. Taranto, S. Member, A real-time voltage instability identification algorithm based on local phasor measurements, IEEE Trans. Power Syst. 23 (3) (2008) 1271–1279.
[16] G.N. Taranto, C. Oyarce, S. Corsi, Further investigations on a phasor measurement-based algorithm utilized for voltage instability awareness, Proceedings of IREP Symposium: Bulk Power System Dynamics and Control - IX Optimization, Security and Control of the Emerging Power Grid, IREP 2013, (2013), pp. 1–8, https://doi.org/10.1109/IREP.2013.6629381.
[17] A. Perez, H. Johannsson, J. Ostergaard, Wind farms generation limits and its impact in real-time voltage stability assessment, 2015 IEEE Eindhoven PowerTech, PowerTech 2015, IEEE, 2015, pp. 1–5, https://doi.org/10.1109/PTC.2015.7232771.
[18] L. Zeni, H. Jóhannsson, A.D. Hansen, P.E. Sørensen, B. Hesselbæk, P.C. Kjær, Influence of current limitation on voltage stability with voltage sourced converter HVDC, 2013 4th IEEE/PES Innovative Smart Grid Technologies Europe, ISGT Europe 2013, (2013), pp. 1–5, https://doi.org/10.1109/ISGTEurope.2013.6695271.
[19] M. Sarkar, M. Altin, P.E. Sørensen, A.D. Hansen, Reactive power capability model of wind power plant using aggregated wind power collection system, Energies 12 (9) (2019) 1607, https://doi.org/10.3390/en12091607.